Industrial Crops & Products 223 (2025) 120162

Contents lists available at ScienceDirect

Industrial Crops & Products

journal homepage: www.elsevier.com/locate/indcrop

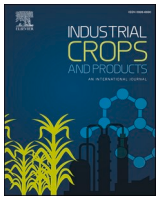

Ni-MOFs and lignin modified biochar: An environmentally-friendly and efficient catalyst for catalytic transfer hydrodeoxygenation of lignin derivatives

Xialin Ji [a,1], Xiaoke Tian [a,1], Mengqing Zhou [a], Changzhou Chen [a,*], Jianchun Jiang [a,b]

[a] Fujian Provincial Key Laboratory of Biomass Low-Carbon Conversion, Academy of Advanced Carbon Conversion Technology, Huaqiao University, Xiamen 361021, China

[b] Institute of Chemical Industry of Forest Products, Chinese Academy of Forestry, Nanjing 210042, China

ARTICLE INFO

Keywords:
Hydrodeoxygenation
Lignin
Metal-organic frameworks

ABSTRACT

In this study, different kinds of lignin, including enzymatic hydrolysis of lignin (EHL), alkaline lignin (AL), kraft lignin (KL) and sodium lignosulfonate (LS) were investigated as precursor to prepare Ni@BTC@X (X= EHL, AL, KL, LS) catalysts using a traditional hydrothermal method with Ni-MOF for HDO upgrading of lignin derivative vanillin (VAN) to generate high value chemical 2-methoxy-4-methylphenol (MMP). The catalytic performance of these catalysts was investigated under different reaction conditions, and it was explored that the conversion of VAN was close to 100 % and the MMP yield was close to 90 % under the optimal conditions (Ni@BTC@LS catalyst, 220 ℃, 4 h, isopropanol, 2 MPa N_2). Various physical-chemical characterization results verified that the effects of active sites Ni, porous structure of lignin biochar support and electronic properties of the catalysts played a significiant role in HDO of lignin derived VAN. Additionally, synergistic effect of the highly homogeneously dispersed oxygen vacancies and acidic sites also promoted the VAN conversion efficiency. This work developed a strategy combing the advantages of MOFs and biomass derived substrates for manufacturing novel lignin/MOFs materials in the catalytic field.

1. Introduction

Lignin, a complex and highly abundant biopolymer found in the cell walls of plants, is recognized for its substantial availability and renewable nature (Chio et al., 2019; Espinoza-Acosta et al., 2018; Li et al., 2015; Rajesh Banu et al., 2019; Sun et al., 2018). Its chemical structure, characterized by various functional groups such as hydroxyl, methoxy, and aromatic rings, provides it with unique properties that are beneficial in catalytic applications (Giummarella et al., 2019; Ma et al., 2024b; Ntakirutimana et al., 2022; Xue et al., 2024; Zhang and Naebe, 2021). One of the key advantages of lignin is its inherent stability and robustness under harsh reaction conditions. Additionally, its high surface area and rich chemical functionality make it an attractive candidate for modification and functionalization, enabling the creation of composites with enhanced catalytic properties. Furthermore, lignin's renewable nature aligns well with the principles of green chemistry, offering an environmentally friendly alternative to conventional non-renewable resources (Chen et al., 2021b, 2021c, 2020).

Metal-organic frameworks (MOFs) are a category of porous substances made up of metal ions or clusters that are interconnected by organic ligands, resulting in a three-dimensional structure. These materials are renowned for their exceptionally high surface areas, tunable porosity, and the ability to host a variety of functional groups (Mo et al., 2022; Moayed Mohseni et al., 2022; Qian et al., 2021; Sabzehmeidani et al., 2024; Wang et al., 2022). The versatility of MOFs in terms of structure and composition allows for precise control over their catalytic properties, making them highly effective in a wide range of chemical transformations. One of the principal advantages of MOFs is their high surface area and large pore volumes, which facilitate the adsorption and activation of reactants. Their tunable nature allows for the incorporation of specific active sites that can enhance reaction selectivity and efficiency. Additionally, MOFs can be designed to exhibit catalytic properties that are not achievable with other materials, making them invaluable in heterogeneous catalysis (Chen et al., 2021a; Xia et al.,

* Corresponding author.
E-mail address: chenchangzhou@hqu.edu.cn (C. Chen).
[1] X.J. and X.T. contributed equally.

https://doi.org/10.1016/j.indcrop.2024.120162
Received 6 August 2024; Received in revised form 10 November 2024; Accepted 26 November 2024
Available online 29 November 2024

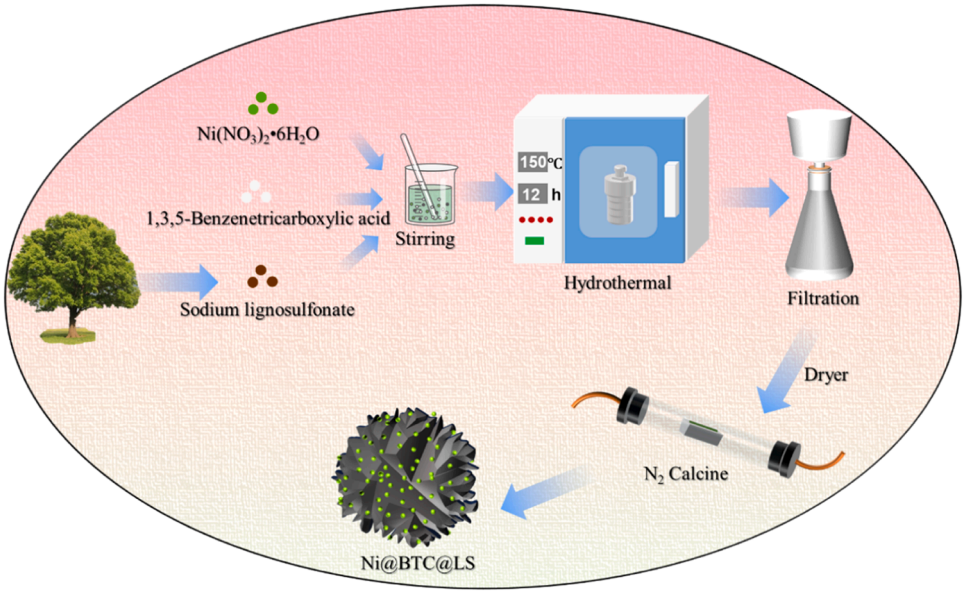

Fig. 1. The detailed preparation progress.

2021; Zhou et al., 2022a).

When combined, lignin and MOFs can exploit their respective strengths to create a composite material with enhanced catalytic properties. Lignin's high surface area and functional groups can provide anchoring sites for MOFs, while MOFs' tunable structures and high surface areas can further enhance the interaction with lignin. This combination can lead to a composite material that not only benefits from the stability and renewability of lignin but also from the advanced catalytic features of MOFs. Lignosulfonate (LS) contains numerous hydrophilic groups such as sulfonate and phenolic hydroxyl groups. Using the hydrophilic groups of lignosulfonates (especially sulfonates), lignosulfonates can form coordination structures with a variety of metal ions, making them an ideal organic ligand. Furthermore, the sulfonate groups on lignosulfonates can provide an intrinsic sulfur source to form sulfur self-doping, which in turn modulates the electronic structure of the monoatomic active site, resulting in higher catalytic activity(Chen et al., 2023). The interaction between lignin and MOFs can result in a material with improved stability and catalytic efficiency (Chen et al., 2024a; Ge et al., 2023; Wu et al., 2024). For instance, the MOF component can enhance the catalytic performance by providing specific active sites and high surface area, while the lignin component can offer structural stability and additional functional groups that interact synergistically with the MOF framework. This synergistic effect can be particularly advantageous in complex catalytic reactions, where multiple steps and functionalities are required. Wu et al. (Wu et al., 2024) introduced an innovative approach for synthesizing N-doped catalysts derived from lignin-MOF, achieving a remarkable 100 % conversion of vanillin and a 92 % yield of 2-methoxy-4-methylphenol (180°C, 0.5 MPa nitrogen, for 2 hours). Additionally, the same research group (Ge et al., 2023) developed a range of catalysts utilizing MOFs as structure-directing agents and lignin as a sustainable carbon source through a straightforward hydrothermal method. Among these, Co/C-EL-0.5–500 demonstrated superior catalytic hydrotreatment performance, resulting in a complete conversion of guaiacol and a 90 % yield of cyclohexanol. In our previous study (Chen et al., 2024a), We engaged in the preparation of kraft lignin integrated with ZIF-67 to create kraft lignin biochar-based carbon materials (Co@NPC-KLB). These innovative carbon materials were employed for the hydrodeoxygenation of lignin-derived bio-oil, aimed at producing valuable fuels and chemicals. Remarkably, the process achieved nearly 100 % conversion of vanillin and 88.49 % conversion of 2-methoxy-4-methylphenol at 240 °C in ethanol, without the need for extra H_2 gas. In recent years, MOF and lignin composite materials have become increasingly popular in various fields, and it is also worth further developing new composite materials and new application areas.

In this work, different kinds of lignin, including enzymatic hydrolysis of lignin (EHL), alkaline lignin (AL), kraft lignin (KL) and sodium lignosulfonate (LS) were investigated as precursor to prepare Ni@BTC@X (X= EHL, AL, KL, LS) catalysts using a traditional hydrothermal method with Ni-MOF for hydrodeoxygenation upgrading of vanillin to generate high value chemical 2-methoxy-4-methylphenol. Usually, lignin separated from paper waste liquid is reacted with sodium bisulphite to produce lignosulfonate, which undergoes high-pressure catalytic oxidation under alkaline conditions, and vanillin is obtained after extraction and refinement. The vanillin used in this experiment was purchased directly from a pharmaceutical company. The MOF component provided active sites and enhanced the catalytic activity, while lignin component offered stability and additional functional groups that could aid in the activation of reactants. This combination could lead to improved reaction rates, higher yield, and better overall yields of MMP. This study presented a strategy that leveraged the benefits of metal-organic frameworks (MOFs) and biomass-derived lignin to create innovative lignin/MOF materials for catalytic applications.

2. Experimental

2.1. Materials

Enzymatic hydrolysis of lignin (EHL), alkaline lignin (AL) and kraft lignin (KL) were sourced from the domestic chemical market. Key chemicals provided by Aladdin Industrial Co., Ltd. included ethanol (99.0 %), isopropyl alcohol (99.0 %), N, N-Dimethylformamide (≥ 99.0 %), methanol (99.0 %), and n-propyl alcohol (99.5 %). Additional compounds like 4-Hydroxy-3-Methoxybenzaldehyde (vanillin, 99 %) and 1,3,5-benzenetricarboxylic acid (≥ 99 %) were acquired from Titan Technology Co., Ltd. Sodium lignosulfonate and Nickel (II) nitrate hexahydrate (99 %) were from Maclean's Biochemical Co., Ltd., while N_2 (99.999 %) was obtained from Fujian, Xiamen local Gas Co., Ltd.

Table 1
BET results of the Ni@BTC@X.

Samples	S_{BET}[a] (m^2/g)	V_{Pore}[a] (cm^3/g)	$D_{Average}$[a] (nm)
Ni@BTC@LS	81.577	0.175	8.571
Ni@BTC@KL	206.666	0.298	5.769
Ni@BTC@AL	129.834	0.325	10.005
Ni@BTC@EHL	171.077	0.312	7.288

[a] Determined by BET method.

2.2. Synthesis of different Ni@BTC@X catalysts

A mixture of 2.95 g of $Ni(NO_3)_2{\cdot}6\,H_2O$ and 2.1 g of 1,3,5-benzenetricarboxylic acid was stirred in 60 mL of N,N-dimethylformamide for 2 hours. Following this, 1 g of lignin (either LS, KL, AL, or EHL) was incorporated, and the mixture was stirred for an additional hour. The resulting solution was then subjected to hydrothermal treatment at 150°C for 12 hours. After the reaction, the solution underwent diafiltration, and the resulting filter cake was rinsed with deionized water and methanol before being dried at 90°C. The dried samples were subsequently calcined in a tube furnace at 500°C for 2 hours while maintaining in a nitrogen flow of 30 sccm. The synthesized catalysts were designated as Ni@BTC@X, where X corresponds to LS, KL, AL, or EHL, with the synthesis procedure for the Ni@BTC@LS catalyst depicted in Fig. 1.

2.3. Catalyst structural characterizations

All physical and chemical characterization methods and information mentioned in the paper can be found in the supporting information.

2.4. Catalyst reactivity evaluation

In a 25 mL high-pressure reactor, a specified amount of catalyst and 100 mg of VAN were subjected to the HDO process in various H-donor solvents. The reactor was inserted with N_2 for 3 times in order to eliminate air. Desired temperature and stirring rate were then set. After the reaction, the reactor was cooled to room temperature in an ice bathing, and inserted gas then was released. The reacted solution was analyzed for component content using gas chromatography/mass spectrometry (Fuli, GC9790 Plus). The result was calculated employing defined formulas (1) and (2).

$$Conversion = \frac{mole\ of\ reacted\ substrate}{total\ mole\ of\ vanillin\ feed} * 100\% \quad (1)$$

$$Yield\ of\ product = \frac{mole\ of\ product}{mole\ of\ converted\ vanillin\ feed} * 100\% \quad (2)$$

In addition, a series of conditions such as dosage, temperature, N_2 pressure, hydrogen supply solution, etc. were varied to evaluate the influence of different catalysts over different conditions.

3. Discussions

3.1. Characterization of catalysts

As displayed in Fig. 2a, N_2 adsorption-desorption isotherms for Ni@BTC@X catalysts were revealed as type IV with a hysteresis loop in the P/P0 range of 0.4–1.0, which was typical adsorption-desorption isotherm curves characteristics of mesoporous materials (Guo et al., 2024). The Ni@BTC@X catalysts also existed an H3 type hysteresis loop, H3 type hysteresis curve was usually found in interstitial layered aggregates, mesoporous or macroporous materials (Cychosz et al., 2017). The above results indicated that the catalysts contained mesoporous structure existence. The textural properties of the Ni@BTC@X catalysts were shown in Table 1. BET surface areas of Ni@BTC@LS, Ni@BTC@KL, Ni@BTC@AL, Ni@BTC@EHL were 81.58, 206.67, 129.83 and 171.08 m^2/g, respectively. It could be suggested from the above results that BET surface area of Ni@BTC@LS was small compared with that of Ni@BTC@KL, Ni@BTC@AL, Ni@BTC@EHL. Different lignin compositions and structures result in different specific surface areas. Higher polymerised lignin may form a denser and denser char structure, resulting in a smaller specific surface area for Ni@BTC@LS than the other three catalysts. (Yue et al., 2020). In addition, the isotherms significantly upraised in the range of 0.5–0.9 P/P_0, indicating an increase in the porosity of Ni@BTC@X. The pore size distribution curve of Fig. 2b also indicated occurrence of mesopores around 4.7 nm. The analysis of pore size distribution revealed that the pore size had minimal influence on the catalytic activity, since all three catalysts displayed mesoporous characteristics, with average pore sizes between 5.77 and 10.00 nm, as depicted in Fig. 2b. (Guo et al., 2023).The functional distribution on the catalyst surface was further characterized by SEM.

In this study, the catalysts were constructed using a solvothermal strategy and then were all prepared by calcination under nitrogen atmosphere. During the calcination process, lignin acts as a carbon source (Ge et al., 2023). The internal metal active site structure (crystal phase), surface states and valence states of the catalysts with different lignin additions were further analyzed and results were displayed in Fig. 3a. It was observed that diffraction peaks at 44.2°, 51.5° and 75.9° appeared for all samples were in agreement with the previous literature (Chen

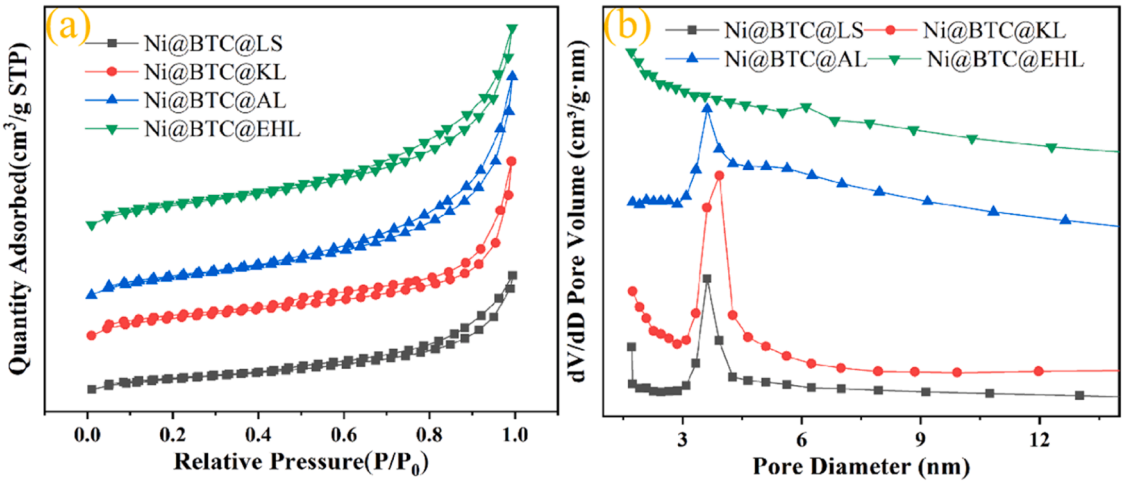

Fig. 2. (a) The N_2 adsorption-desorption isotherms and (b) pore diameter distribution curves.

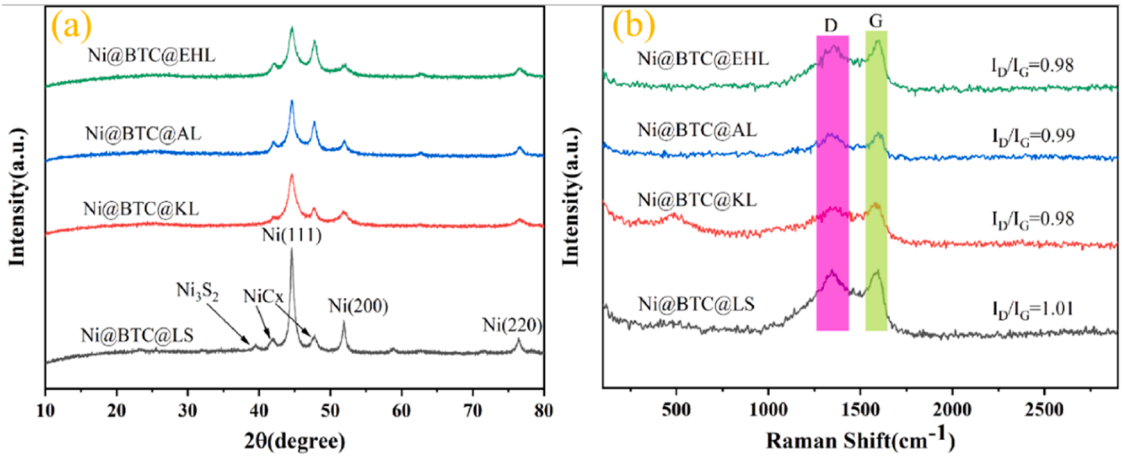

Fig. 3. XRD patterns and Raman spectrums.

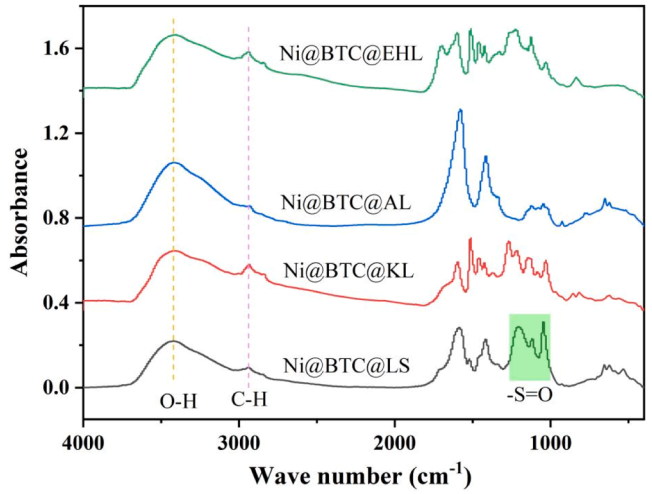

Fig. 4. FT-IR spectra of LS, KL, AL, and EHL.

et al., 2024b). For Ni@BTC@LS catalyst, as indicated by the standard JCPDS file (PDF#06–0697), the two diffraction peaks observed at 42.00° and 45.90° corresponded to the (006) and (113) crystal planes of rhombohedral (RH) NiCx. The standard JCPDS file (PDF#04–0850) for metallic Ni revealed typical diffraction patterns from the (111), (200), and (220) crystal planes (Cao et al., 2022; Ma et al., 2023; Yang et al., 2020), respectively. Moreover, the 2θ values at 39.0° was indexed to the (021) planes of Ni_3S_2(Chen et al., 2021b). The Ni diffraction peak positions of the different samples showed minimal variation, indicating that the incorporation of various lignin precursors did not significantly impact the growth of the Ni-MOF. In contrast to the Ni@BTC@LS sample, the Ni diffraction peak intensities in the other three samples were markedly diminished. The results indicated that Ni@BTC@LS catalysts have stronger crystallinity of Ni relative to the other three catalysts. This observation indicated a reduction in the degree of crystallinity and the overall content of metal Ni. Furthermore, no Ni-related oxides or hydroxides were detected by XRD, confirming that the in situ synthesized α-$Ni(OH)_2$ was completely converted into a Ni-based MOF structure. The characteristic peaks of the samples were distinct, and no impurity peaks were observed, demonstrating that the samples prepared via the solvothermal method exhibit strong crystallinity.

Raman spectroscopy provided insights into the crystal defects present in the carbon atoms. In all Ni@BTC@X catalysts, Raman characteristic peaks were identified around 1350 and 1580 cm^{-1} in Fig. 3b, which corresponded to the D band, indicative of amorphous carbon, and the G band, representative of graphitic carbon, respectively. The D band showed the carbon defects in the lattice and the G band reflected the degree of carbonization of the material. For Ni@BTC@LS catalyst, it showed a higher I_D/I_G value (I_D/I_G =1.01) compared to other three catalysts (0.98 for Ni@BTC@KL, 0.99 for Ni@BTC@AL and 0.98 for Ni@BTC@EHL). The ID/IG values represented the strongest peak ratios for D and G bands, suggesting that sodium lignosulfonate precursor showed the least graphitized and exhibited a higher density of defect sites. These abundant surface defects provided accessible active sites, enabling the anchoring of nickel atoms and enhancing their dispersion (Lu et al., 2023; Luo et al., 2022).Thus, enriched carbon defects could significantly enhance the catalytic activity.

The FT-IR spectra of LS, KL, AL, and EHL are shown in Fig. 4. According to the literature(Alwadani and Fatehi, 2019), the absorption peaks between 3400 cm^{-1} - 3100 cm^{-1} and 2930 cm^{-1} - 2300 cm^{-1} correspond to the O-H bond in the phenolic hydroxyl group and the C-H bond in the aldehyde group, respectively. LS showed broad strong absorption peaks at 1200 cm^{-1}-1000 cm^{-1} and -S═O deformation vibrational absorption peaks at 1150 cm^{-1}, 1042 cm^{-1}. None of the other three lignins showed sulfonate absorption peaks. The S element in the sulphonate can provide an intrinsic source of sulphur to form sulphur self-doping, which modulates the electronic structure of the active site of the Ni atom and thus the catalytic hydrogenation activity becomes better.

The surface structure of different catalysts was subsequently examined with scanning electron microscopy, with the results displayed in Fig. 5. The Ni@BTC@LS catalysts exhibited an aggregated spherical flower shape. In our previous study, trimeric acid served as the structure-directing agent to create the uniform spherical structure without the need for additional carbon sources (Chen et al., 2024b). In catalysts with different levels of lignin precursor, the spherical structures were altered and transformed into loose clusters to varying degrees. This indicates that the introduction of lignin precursor into the hydrothermal process adversely affected crystal growth and the growth of spherical structures, especially observed in the cases of KL, AL, and EHL. This observation highlighted that Ni@BTC@LS was more favorable for the hydrodeoxygenation of VAN(Chen et al., 2021a; Li et al., 2022a).

As shown in Fig. S1, the higher degree of aggregation of catalyst particles of catalyst Ni@BTC@KL may lead to the masking of some surface sites, which reduces the activity of the whole catalyst.Catalysts Ni@BTC@AL and Ni@BTC@EHL have an uneven size distribution of Ni particles and fewer Ni particles with respect to catalyst Ni@BTC@LS, which affects the yield and efficiency of the catalytic reaction. The optimal Ni@BTC@LS was then examined using transmission electron microscopy, which was displayed in Fig. 6. The catalyst presented as

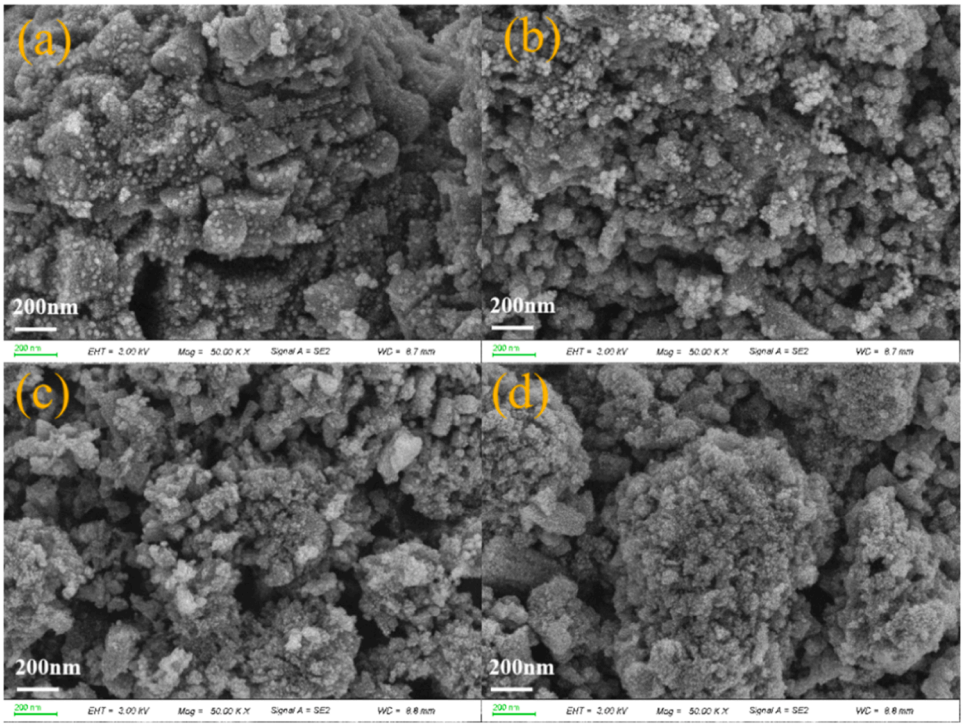

Fig. 5. SEM images of different catalysts (a) Ni@BTC@LS, (b) Ni@BTC@KL, (c) Ni@BTC@AL and (d) Ni@BTC@EHL.

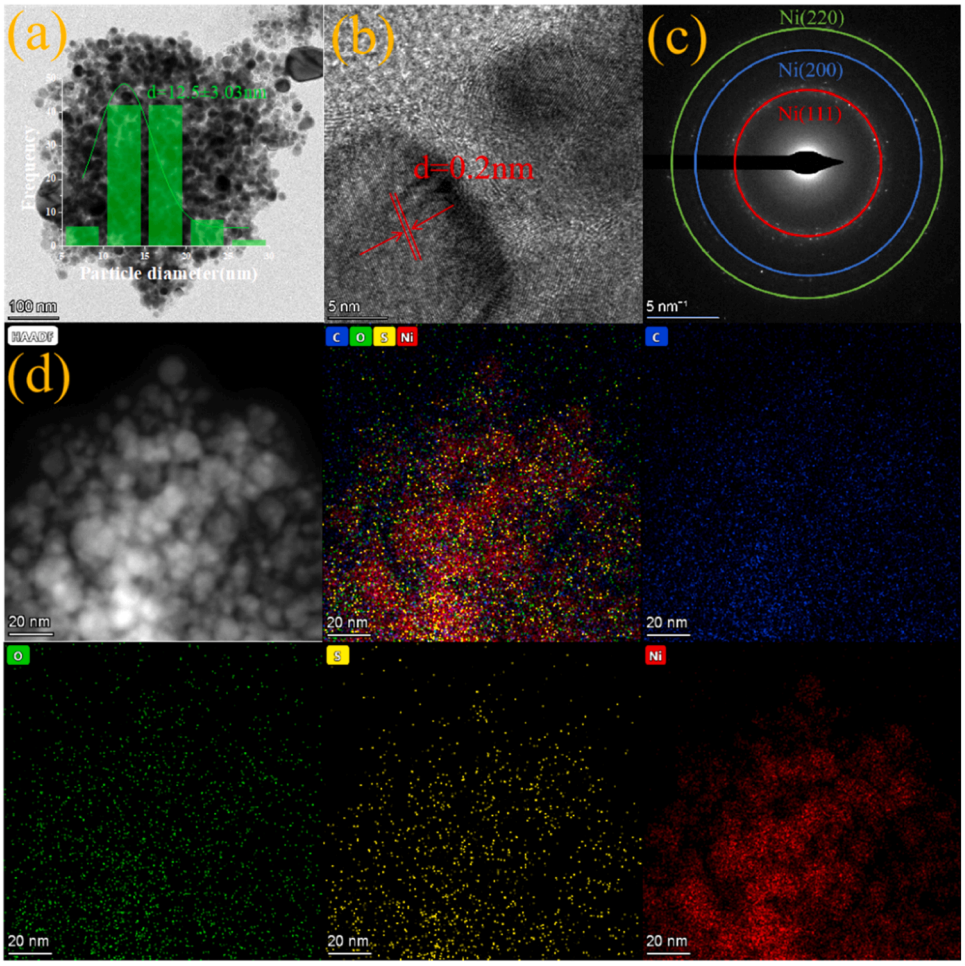

Fig. 6. (a-b) TEM images of Ni@BTC@LS (insert (a), particle size distributions), (c) SAED image of Ni@BTC@LS and mapping images of Ni@BTC@LS(d).

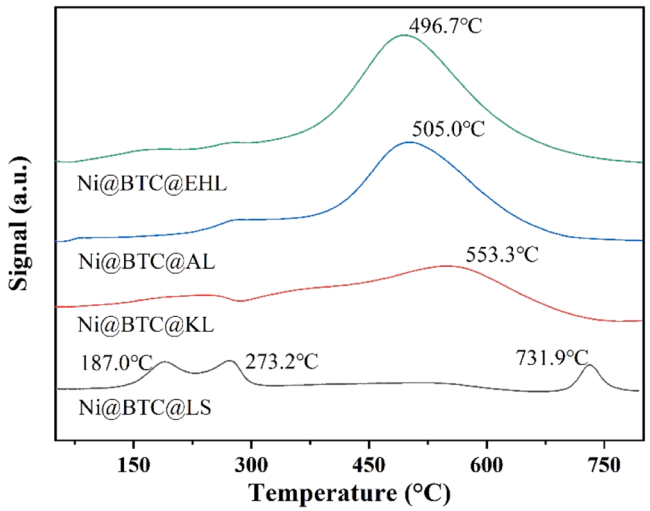

Fig. 7. H_2-TPR of Ni@BTC@X catalysts.

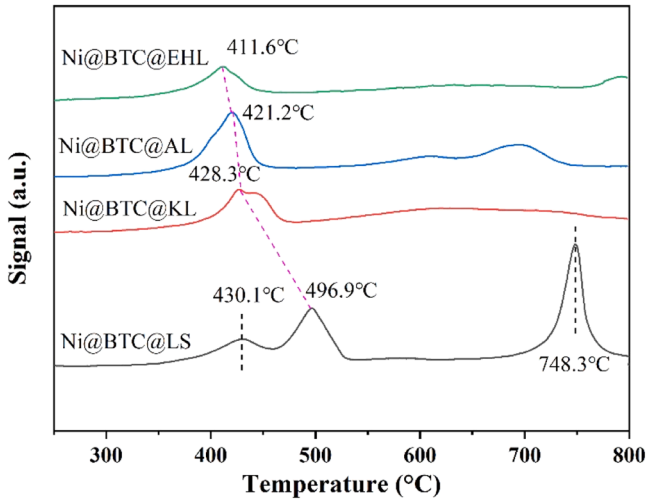

Fig. 8. NH_3-TPD of Ni@BTC@X catalysts.

carbon-loaded particles featuring relatively thin carbon shells on their surfaces. These particles were fairly uniform in size and well-distributed, with an approximate diameter of 12.5 nm. HRTEM images revealed distinct lattice fringes, with the most pronounced lattice spacing measuring around 0.2 nm, which corresponded to the Ni (111) crystal planes (Gao et al., 2022; Zhai et al., 2023). Fig. S2 shows that Ni@BTC@LS has a relatively good dispersion, and better dispersion usually improves the catalytic effect of the catalyst. This observation aligned with the results obtained from X-ray Diffraction (XRD) analysis presented in Fig. 3a. Moreover, the Selected Area Electron Diffraction (SAED) image in Fig. 6c obviously showed three diffraction rings. The innermost ring, corresponding to Ni (111) plane, exhibited the highest intensity among the diffraction rings. Additionally, the elemental mapping image of Ni@BTC@LS, shown in Fig. 6d, indicated a concentration of Ni within the particles. This observation confirmed the agglomeration of metallic Ni in the catalyst, while also demonstrating a uniform distribution of S elements, consistent with the XRD findings for Ni@BTC@LS.

In addition, the reducibility of the prepared Ni@BTC@X catalysts was studied by H_2-TPR (Zhou et al., 2022b). Fig. 7 displayed the H_2-TPR curves of Ni@BTC@X. A reduction peak was observed for Ni@BTC@KL, Ni@BTC@AL and Ni@BTC@EHL between 300 °C and 600 °C, which followed the order: Ni@BTC@KL (553.3°C) > Ni@BTC@AL (505.0°C) > Ni@BTC@EHL (496.7°C). For Ni@BTC@LS catalyst, The H_2-TPR curve showed a broad band out around 150 ℃ and 300 °C that can be split into two typical depletion peaks, with the peak around 250–300 °C corresponding to the reduction of nickel monoxide on the carbon carrier. In addition, a typical reducibility temperature at 719.3 °C was observed, which indicated a tight integration between active sites and lignin biochar.

Table 2
Strong acidity of all catalysts.

Catalysts	Strong Acidity (cm^3/g STP) (>400 ℃)
Ni@BTC@LS	67.81
Ni@BTC@KL	48.26
Ni@BTC@AL	38.25
Ni@BTC@EHL	23.62

Fig. S3 illustrated the TG curves for the Ni@BTC@X catalysts. Notably, Ni@BTC@LS exhibited a slower rate of weight loss compared to the other catalysts. In contrast, the weight loss of Ni@BTC@KL, Ni@BTC@AL, and Ni@BTC@EHL catalysts was more significant before reaching 500 °C, after which the weight loss rate diminished. Consequently, a calcination temperature of 500 °C was selected for catalyst preparation in this study. This study also examined the distribution of acidity and the quantity of acidic sites on the catalyst surface through NH_3-TPD spectroscopy. The desorption peaks of ammonia in the NH_3-TPD analysis could be classified into three categories of acidic sites: weak acid (< 200°C), medium acid (200–400°C) and strong acid (> 400°C) (Liu et al., 2020; Zeng et al., 2023). As illustrated in Fig. 8, all catalysts exhibited peak desorption above 400°C, suggesting observation of strong acid sites. The surface acidity values obtained from the NH_3-TPD experiments were presented in Table 2 and Table S1; notably, the acidity value for Ni@BTC@LS was 67.81 cm^3/g STP, significantly surpassing those of the other catalysts. Catalysts with a greater number of acidic sites demonstrated enhanced efficiency in the hydrodeoxygenation of vanillin, highlighting the critical role that acidic sites play in the HDO performance of vanillin.

Fig. 9 and Fig. S4 presented the XPS of different Ni@BTC@X catalysts. In C 1 s spectrum of Ni@BTC@X catalyst in Fig. 9a, three fitted peaks corresponded to sp^2, sp^3, and C-O bonds, respectively. Regarding the oxygen species in Fig. 9b, the three peaks in the O 1 s spectrum are attributed to lattice oxygen (O_L), oxygen vacancies (O_V), and oxygen adsorbed on the O_V surface (O_C) (Chen et al., 2018; Zhang et al., 2023). The results suggested that Ni@BTC@LS possessed a greater concentration of oxygen vacancies compared to several other three catalysts. These vacancies may serve as active sites in catalytic reactions, facilitating the activation of reactants and the hydrodeoxygenation process. Additionally, the presence of O vacancies was likely to improve acidity of the catalyst, aligning with the findings from the NH_3-TPD analysis (Vernekar et al., 2021; Zhang et al., 2021). Fig. 9c displayed Ni 2p spectra of Ni@BTC@LS, where the peaks at 851.9 and 854.3 eV attributed to Ni^0 and Ni^{2+}, respectively, along with a satellite peak at 860.4 eV (Li and Xia, 2024). The S 2p spectrum of Ni@BTC@LS in Fig. 9d showed peaks around 161.4 and 168.1 eV, which corresponded to Ni-S and C-S bonds, respectively. Overall, the XPS results indicated the successful synthesis of Ni@BTC@LS catalyst, which exhibited a uniform distribution of Ni, S, O elements and demonstrated a good catalytic activity.

3.2. Catalytic performance

3.2.1. Screening of catalysts

In this study, we synthesized monometallic Ni@BTC@X catalysts utilizing various lignin samples as carbon sources. To effectively compare the catalytic activities of the different catalysts, we assessed their performance in the HDO of VAN. A range of reaction products was identified, including 2-methoxy-4-methylphenol (MMP), vanillyl

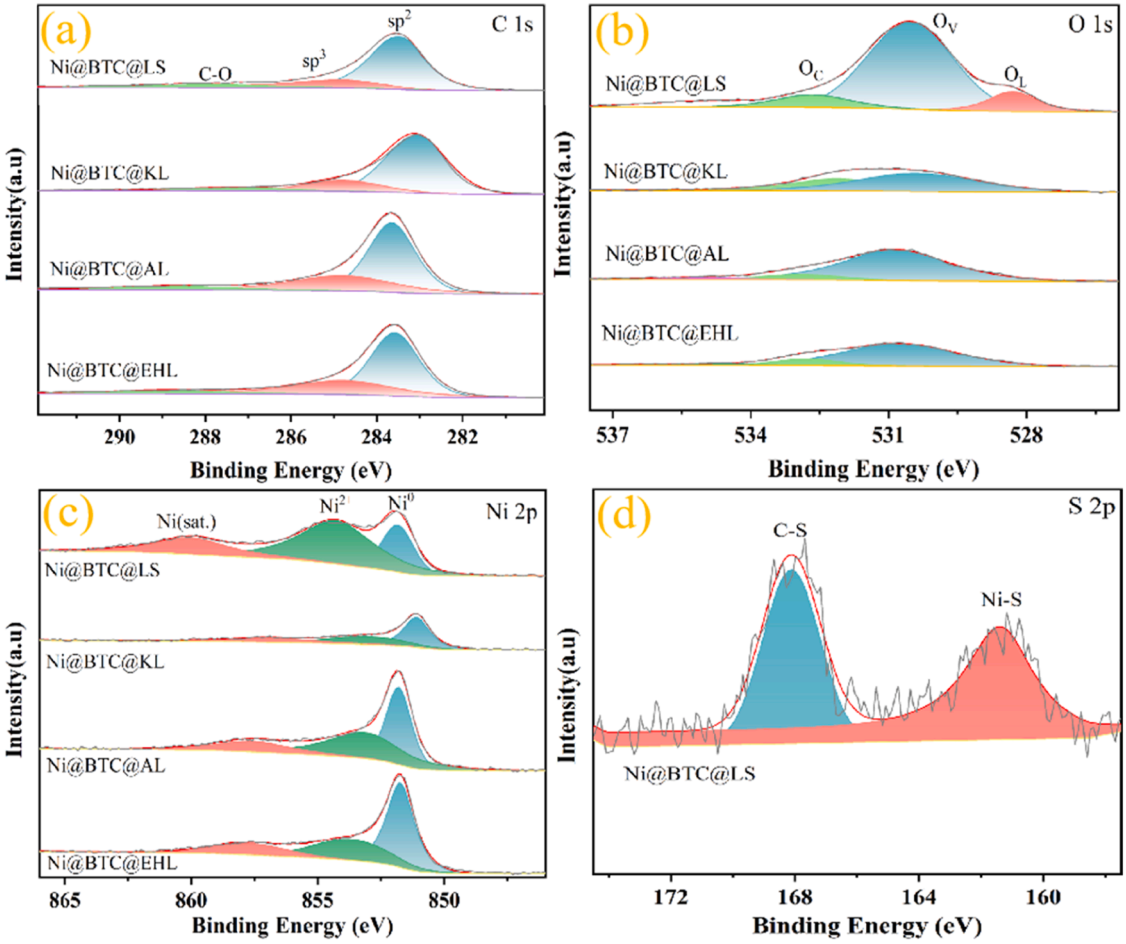

Fig. 9. XPS spectra of (a) C 1 s, (b) O 1 s, (c) Ni 2p of the Ni@BTC@X catalysts. and (d) S 2p of the Ni@BTC@LS catalyst.

Table 3
Experiments on different Ni@BTC@X.

Catalyst	Conversion/%	Yield/%			
		VAL	MMP	HMA	GUA
Ni@BTC@LS	97.95	0.36	85.99	3.25	8.35
Ni@BTC@KL	91.60	2.6	46.97	11.15	30.88
Ni@BTC@AL	97.68	1.12	59.48	3.83	33.25
Ni@BTC@EHL	99.18	5.8	48.8	19.58	25

alcohol (VAL), 4-(isopropoxymethyl)-2-methoxyphenol (HMA), and guaiacol (GUA). The results demonstrated that all catalysts examined exhibited significant catalytic efficacy in the hydrodeoxygenation of VAN, with conversion rates exceeding 90 %. However, the yields of primary product MMP varied notably. Among the catalysts evaluated, the Ni@BTC@LS catalyst, utilizing sodium lignosulfonate as the carbon source, displayed the most effective hydrogenation and deoxygenation performance for VAN, achieving an impressive MMP yield of 85.99 %, as indicated in Table 3. As shown in Fig. S5, the catalytic effect of simultaneous addition of BTC and LS was significantly improved over that of individual addition. When Ni@BTC@KL catalyst was used as the VAN dehydrogenation catalyst, the conversion of VAN was 91.60 %, the yield of MMP was 46.97 % and the yield of by-products was 42.03 %. It indicates that the catalytic activity of Ni@BTC@KL catalyst for VAN dehydrogenation is low. Ni@BTC@AL and Ni@BTC@EHL played low to moderate role at 220°C, 2 MPa N_2 pressure and 4 h. According to the NH_3-TPD results in Fig. 8, the Ni@BTC@LS catalyst with more acidic sites can activate the reactants and enhance their adsorption capacity for

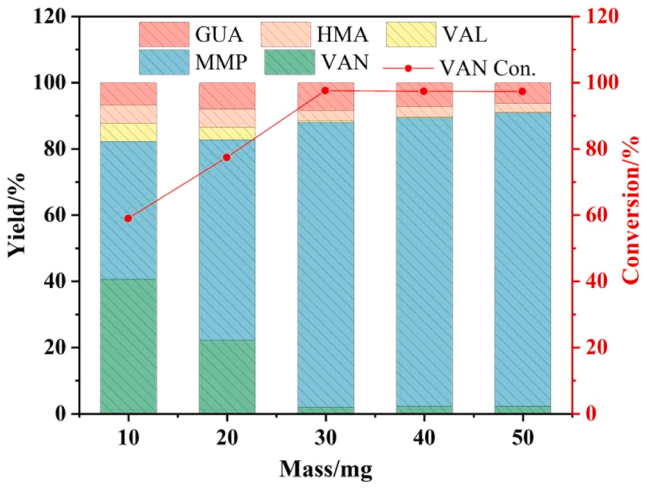

Fig. 10. Influence of different catalyst mass.

H atoms. Thus, the catalytic activity of the catalyst is improved. Consequently, Ni@BTC@LS as then selected as the optimized catalyst for the subsequent experiments.

Condition: Substrate 0.1 g, Cat. 0.03 g, 15 mL isopropyl alcohol, 220 ℃, four hours, 2.0 MPa nitrogen pressure.

3.2.2. *Different affecting factors*

The catalytic efficiency on the HDO of VAN with varying masses of

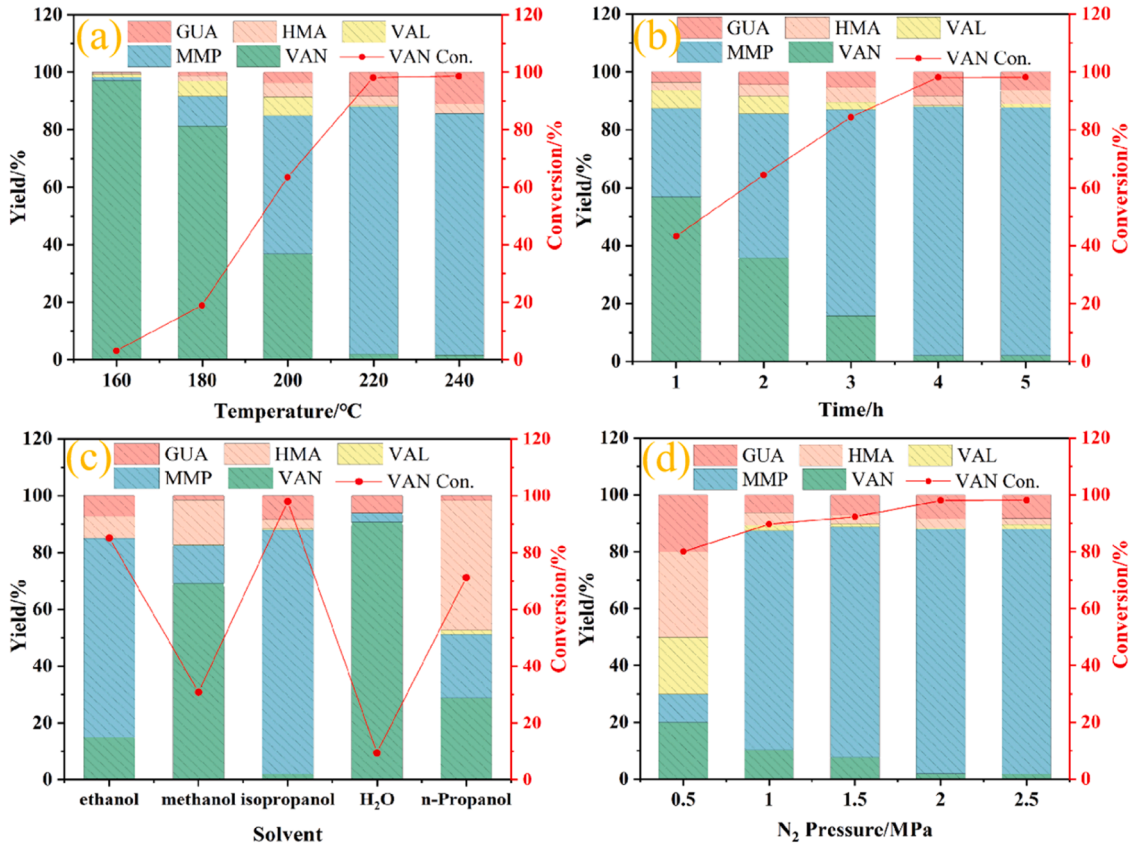

Fig. 11. VAN hydrodeoxygenation conversion and product yield over different conditions.

catalyst are depicted in Fig. 10. According to the experimental findings, mass of optimal Ni@BTC@LS ranged from 10 to 30 mg. With an increase in catalyst mass, an upward trend in VAN conversion was observed. The conversion rate reached an impressive 97.95 % at 30 mg of Ni@BTC@LS catalyst, resulting in a target product yield of 85.99 % for 2-methoxy-4-methylphenol (MMP). However, when the catalyst mass exceeded 30 mg, there was no significant improvement in VAN conversion, despite a marginal increase in MMP yield. Therefore, we determined 30 mg to be the optimal amount of Ni@BTC@LS catalyst, as it achieved a favorable balance between maximum conversion and yield while ensuring efficient utilization of the catalyst.

The conversion pathway for the hydrodeoxygenation of vanillin was further investigated by examining various reaction parameters in Fig. 11 to identify the optimal conditions for catalytic HDO using the Ni@BTC@LS catalyst. To evaluate the influence of reaction temperature, we conducted the HDO process from 160 °C to 240 °C, as illustrated in Fig. 11a. The results indicated that temperature showed an important impact on VAN conversion. At 160 °C, the conversion rate was only approximately 2.84 %. Increasing the temperature to 200 °C raised the conversion to about 63.24 %. A further temperature increasing to 220 °C resulted in a substantial conversion of nearly 97.95 %, with the yield of the target product MMP also improving to 85.99 %. The findings demonstrated a linear correlation between MMP yield and temperature, suggesting that higher temperatures facilitated more effective hydrodeoxygenation of VAN to MMP. Notably, intermediate compound valdecoxib was eliminated with the temperature rising above 200 °C, indicating that hydrogenation primarily occurred at relatively lower temperatures (Wu et al., 2024). Additionally, the yield of GUA rose with temperature, reaching 11 % at 240 °C. However, beyond 220 °C, VAN conversion and MMP yield showed little change, while GUA production increased. Considering the energy consumption, we ultimately determined that the temperature of 220 °C was an optimal temperature. in addition, the reaction time also significantly influenced the conversion rate (Ji et al., 2024). To evaluate the impact of reaction time, we kept the temperature constant at the optimal level of 220 °C in Fig. 11b. At 1 hour of reaction time, VAN conversion was only 43.13 %, with an MMP yield of 30.56 %. Extending the reaction time to 4 hours resulted in a rapid increase in VAN conversion to nearly 100 % and a sharp rise in MMP yield to 85.99 %. Experimental results clearly indicated that MMP yield increased with extended reaction time from 1 hour to 4 hours. However, yield for MMP and GUA was also dependent on reaction time. As reaction time rose over 4 hours, VAN conversion and MMP yield slightly changed, but GUA by-products increased. To optimize MMP yield, we chose 4 hours as an additional optimal condition for the HDO process.

Besides the reaction temperature and time, the selection of hydrogen donor solvent also had a considerable impact on catalytic activity (Niu et al., 2016; Xie et al., 2024). Under the previously established optimal conditions, we explored the impact of different solvents on the VAN hydrogenation reaction (Fig. 11c). CH_3OH, CH_3CH_2OH, H_2O, n-propyl alcohol, and isopropyl alcohol were selected as reaction solvents. The solvent served both as a reaction substrate and hydrogen-donor solvent. As illustrated in Fig. 11c, the use of methanol as a solvent led to approximately 31 % conversion of VAN and a yield of 16 % for HMA. This was likely attributed to a low dehydrogenation efficiency associated with short chain alcohol, which favor etherification reactions instead. When ethanol was used, the conversion of VAN increased to approximately 85 % with a 70 % yield of MMP. In contrast, water as a solvent resulted in a mere 10 % conversion, likely due to potential leaching of active metals from the catalyst, lowering catalytic activity. The use of n-propanol yielded nearly 71 % conversion, while isopropanol achieved close to 100 % conversion and an MMP yield of 85.99 %. Consequently, isopropanol was selected as the hydrogen donor solvent for our experiments. Traditional HDO process typically utilized

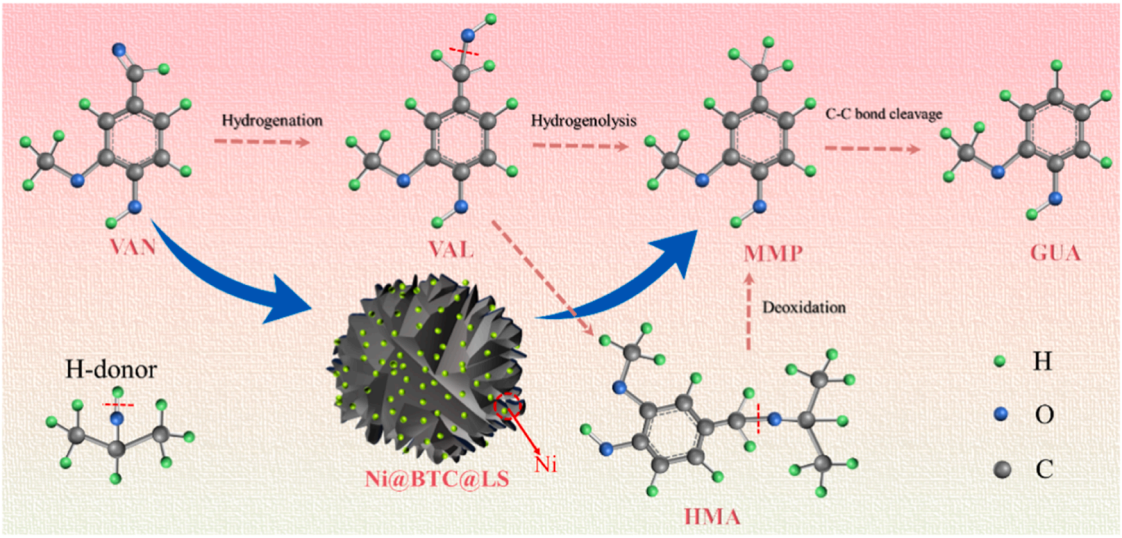

Fig. 12. The reaction pathway for HDO of VAN over Ni@BTC@LS.

H_2 as a hydrogen source (Gao et al., 2022). However, H_2 use posed safety risks and contributed to costs. Therefore, we selected isopropanol as the hydrogen-supplying solvent for the HDO of VAN under a N_2 atmosphere. Under optimal conditions, the influence of varying N_2 pressures was studied, as illustrated in Fig. 11d. High conversion rates of VAN were observed across different N_2 pressures, with the highest MMP yield achieved at 2 MPa N_2. Hence, we selected 2 MPa N_2 as the optimal pressure condition. To minimize repetition, optimal reaction conditions were determined as follows: Ni@BTC@LS catalyst, 220 °C, 4 hours, isopropanol, and 2 MPa N_2.

3.3. Pathway for the conversion of VAN

It was significant to explore the detailed conversion mechanism. During the process of vanillin hydrodeoxygenation, hydrogen atoms extracted from isopropanol interacted with O atom of the -CHO group in vanillin. It was known that the conversion of VAN to MMP was a multifaceted process, which encompassed direct hydrogenation, hydrodeoxygenation, and demethoxylation. The by-product guaiacol was then generated through the subsequent hydrogenation and demethylation of target product MMP. Taking into account the structure of HMA, it was deduced that HMA was generated through dehydration of vanillyl alcohol (VAL) and isopropanol. This process involved hydrogen transfer reactions that promoted formation of ether bonds (Li et al., 2022b; Ma et al., 2024a). As shown in Fig. 11b, the extension of the reaction time from 1 h to 3 h resulted in a decrease in VAL yield to 2.56 % and an increase in MMP yield to 71.21 %, indicating that VAL was identified as an intermediate, and this trend increased at a longer reaction time of 5 h. The results showed that the catalytic process involved the hydrogenation of vanillin to HMA and the hydrolysis of HMA by isopropanol, which is the substrate of the reaction. The results suggest that the catalytic process involves the hydrogenation of vanillin to VAL, the partial conversion of VAL to HMA using isopropanol as the reaction substrate, and the hydrolysis of VAL and HMA to give MMP. As shown in Fig. 12, the conversion route of VAN can be outlined as follows: VAN → VAL → HMA → MMP → GUA, illustrating an order of product formation at high temperatures.

4. Conclusion

In conclusion, we explored various types of lignin as precursors for the preparation of different Ni@BTC@X materials (where X referred to EHL, AL, KL, or LS) using a traditional hydrothermal method combined with Ni-MOF. The objective was to realize the HDO of VAN into high-value chemical MMP. We assessed catalytic activity of different Ni@BTC@X materials over different conditions, finding that, under optimal settings (utilizing the Ni@BTC@LS catalyst at 220 °C for 4 hours in isopropanol with 2 MPa N_2), the conversion of VAN reached nearly 100 %, with MMP yields approaching 90 %. Physical-chemical characterization results confirmed that the active nickel sites, the porous structure of the lignin biochar support, and the electronic properties of Ni@BTC@LS catalyst played crucial roles for the HDO process of VAN. Additionally, the synergistic influence of uniformly dispersed oxygen vacancies and acidic sites further enhanced VAN conversion efficiency. This work presented a strategy that merged the advantages of metal-organic frameworks (MOFs) with biomass-derived substrates, paving a wide way for the exploration of innovative lignin/MOF materials in catalysis.

CRediT authorship contribution statement

Xiaoke Tian: Validation, Investigation. **Xialin Ji:** Writing – original draft, Visualization, Investigation, Data curation, Conceptualization. **Changzhou Chen:** Writing – review & editing, Supervision, Resources, Methodology, Conceptualization. **Mengqing Zhou:** Investigation. **Jianchun Jiang:** Supervision, Funding acquisition.

Declaration of Competing Interest

The authors declare that they have no known competing financial interests or personal relationships that could have appeared to influence the work reported in this paper.

Acknowledgement

We were supported by the Fundamental Research Funds for the Central Universities (ZQN-1216).

Appendix A. Supporting information

Supplementary data associated with this article can be found in the online version at doi:10.1016/j.indcrop.2024.120162.

Data availability

The authors are unable or have chosen not to specify which data has

been used.

References

Alwadani, N.S., Fatehi, P., 2019. Modification of Kraft Lignin with Dodecyl Glycidyl Ether. ChemistryOpen 8, 1258–1266.

Cao, X., Zhao, J., Long, F., Liu, P., Jiang, X., Zhang, X., Xu, J., Jiang, J., 2022. Efficient low-temperature hydrogenation of fatty acids to fatty alcohols and alkanes on a Ni-Re bimetallic catalyst: The crucial role of NiRe alloys. Appl. Catal. B: Environ. 312, 121437..

Chen, C., Chen, W., Zhou, M., Xiong, Y., Ji, X., Zhou, M., Zhang, L., Rao, X., Jiang, J., 2024a. Co-ZIF reinforced kraft lignin biochar as an efficient catalyst for highly selective hydrodeoxygenation of lignin-derived chemicals. Chem. Eng. J. 492, 152353.

Chen, C., Ji, X., Xiong, Y., Jiang, J., 2024b. Ni/Ce co-doping metal–organic framework catalysts with oxygen vacancy for catalytic transfer hydrodeoxygenation of lignin derivatives vanillin. Chem. Eng. J. 481, 148555.

Chen, C., Liu, P., Zhou, M., Li, J., Xia, H., Jiang, J., 2021a. One-step catalytic hydrotreatment of lignin dimer model compounds to cycloalkane and cycloalcohol by spherical metal-organic framework derived NiLa bimetallic materials. J. Energy Inst. 99, 105–119.

Chen, C., Wu, D., Liu, P., Li, J., Xia, H., Zhou, M., Jiang, J., 2021b. Eco-friendly preparation of ultrathin biomass-derived Ni3S2-doped carbon nanosheets for selective hydrogenolysis of lignin model compounds in the absence of hydrogen. Green. Chem. 23, 3090–3103.

Chen, C., Wu, D., Liu, P., Xia, H., Zhou, M., Hou, X., Jiang, J., 2021c. Efficient Ni-based catalysts for the hydrotreatment of lignin dimer model compounds to cycloalkanes/cycloalkanols. React. Chem. Eng. 6, 559–571.

Chen, C., Zhou, M., Liu, P., Sharma, B.K., Jiang, J., 2020. Flexible NiCo-based catalyst for direct hydrodeoxygenation of guaiacol to cyclohexanol. N. J. Chem. 44, 18906–18916.

Chen, Y., Yang, W., Gao, S., Sun, C., Li, Q., 2018. Synthesis of Bi_2MoO_6 Nanosheets with Rich Oxygen Vacancies by Postsynthesis Etching Treatment for Enhanced Photocatalytic Performance. ACS Appl. Nano Mater. 1, 3565–3578.

Chen, Z., Peng, X., Chen, Z., Li, T., Zou, R., Shi, G., Huang, Y., Cui, P., Yu, J., Chen, Y., Chi, X., Loh, K.P., Liu, Z., Li, X., Zhong, L., Lu, J., 2023. Mass Production of Sulfur-Tuned Single-Atom Catalysts for Zn–Air Batteries. Adv. Mater. 35, 2209948.

Chio, C., Sain, M., Qin, W., 2019. Lignin utilization: A review of lignin depolymerization from various aspects. Renew. Sustain. Energy Rev. 107, 232–249.

Cychosz, K.A., Guillet-Nicolas, R., García-Martínez, J., Thommes, M., 2017. Recent advances in the textural characterization of hierarchically structured nanoporous materials. Chem. Soc. Rev. 46, 389–414.

Espinoza-Acosta, J.L., Torres-Chávez, P.I., Olmedo-Martínez, J.L., Vega-Rios, A., Flores-Gallardo, S., Zaragoza-Contreras, E.A., 2018. Lignin in storage and renewable energy applications: A review. J. Energy Chem. 27, 1422–1438.

Gao, J., Cao, Y., Luo, G., Fan, J., Clark, J.H., Zhang, S., 2022. High-efficiency catalytic hydrodeoxygenation of lignin-derived vanillin with nickel-supported metal phosphate catalysts. Chem. Eng. J. 448, 137723.

Ge, F., Xia, H., Li, J., Xue, Y., Su, J., Yang, X., Jiang, J., Zhou, M., 2023. Lignin meets MOFs: Lignin derived metal carbon material for the catalytic hydrotreatment of guaiacol to cyclohexanol. Chem. Eng. J. 473, 145375.

Giummarella, N., Pu, Y., Ragauskas, A.J., Lawoko, M., 2019. A critical review on the analysis of lignin carbohydrate bonds. Green. Chem. 21, 1573–1595.

Guo, H., Chen, Z., Yin, Q., Sun, T., Liu, Y., Ren, G., Li, C., 2023. Waste to wealth: H2S-free fabrication of Fe-ZnS/NC by industrial lignin self S-doping for efficient lignin aerobic oxidation. Appl. Catal. B: Environ. 339, 123129.

Guo, H., Wang, G., Zhang, B., Li, J., Sui, W., Jia, H., Si, C., 2024. Ultrafine Ru nanoparticles deposited on lignin-derived nitrogen-doped carbon nanolayer for the efficient conversion of levulinic acid to γ-valerolactone. Renew. Energy 222, 119954.

Ji, X., Zhou, M., Xiong, Y., Chen, C., Jiang, J., 2024. Renewable biomass-derived hollow carbon sphere for efficient transformation of lignin-derived phenols to high value chemicals. Ind. Crops Prod. 212, 118316.

Li, C., Zhao, X., Wang, A., Huber, G.W., Zhang, T., 2015. Catalytic Transformation of Lignin for the Production of Chemicals and Fuels. Chem. Rev. 115, 11559–11624.

Li, J.T., Xia, S., 2024. Bimetallic NiMo Using MOF-Derived Carbon-Supported Catalysts for the Reaction of Lauric Acid to Alkane. Catal. Surv. Asia. https://doi.org/10.1007/s10563-024-09425-2.

Li, T., Li, H., Li, C., 2022a. Hydrodeoxygenation of vanillin to creosol under mild conditions over carbon nanospheres supported palladium catalysts: Influence of the carbon defects on surface of catalysts. Fuel 310, 122432.

Li, T., Li, H., Li, C., 2022b. Self-support semi-hollow carbon nanosphere supported palladium catalyst for biomass upgrading. Renew. Energy 191, 101–109.

Liu, M., Zhang, J., Zheng, L., Fan, G., Yang, L., Li, F., 2020. Significant Promotion of Surface Oxygen Vacancies on Bimetallic CoNi Nanocatalysts for Hydrodeoxygenation of Biomass-derived Vanillin to Produce Methylcyclohexanol. ACS Sustain. Chem. Eng. 8, 6075–6089.

Lu, K.-L., Yin, F., Wei, X.-Y., Zhu, Z.-J., Li, Z., Li, J.-H., Kong, Q.-Q., Li, L., Zong, Z.-M., 2023. Catalytic hydroconversion of poplar lignin over a nitrogen-doped carbon material-supported nickel prepared by in situ co-pyrolysis. Mol. Catal. 534, 112806.

Luo, B., Zhou, L., Tian, Z., He, Y., Shu, R., 2022. Hydrogenolysis of cornstalk lignin in supercritical ethanol over N-doped micro-mesoporous biochar supported Ru catalyst. Fuel Process. Technol. 231, 107218.

Ma, L., Zhang, G., Dong, Y., Dou, S., Meng, Q., Yan, P., Liu, L., Kong, X., 2023. Hydrodeoxygenation of lignin derivatives over Ni-Re bimetallic catalyst supported on mesoporous carbon sphere. J. Environ. Chem. Eng. 11, 110215.

Ma, L., Zhang, G., Dou, S., Dong, Y., Kong, X., 2024a. WOx boosted hollow Ni nanoreactors for the hydrodeoxygenation of lignin derivatives. Int. J. Biol. Macromol. 269, 132156.

Ma, Q., Yu, C., Zhou, Y., Hu, D., Chen, J., Zhang, X., 2024b. A review on the calculation and application of lignin Hansen solubility parameters. Int. J. Biol. Macromol. 256, 128506.

Mo, F., Zhou, Q., Wang, Q., Hou, Z., Wang, J., 2022. The applications of MOFs related materials in photo/electrochemical decontamination: An updated review. Chem. Eng. J. 450, 138326.

Moayed Mohseni, M., Jouyandeh, M., Mohammad Sajadi, S., Hejna, A., Habibzadeh, S., Mohaddespour, A., Rabiee, N., Daneshgar, H., Akhavan, O., Asadnia, M., Rabiee, M., Ramakrishna, S., Luque, R., Reza Saeb, M., 2022. Metal-organic frameworks (MOF) based heat transfer: A comprehensive review. Chem. Eng. J. 449, 137700.

Niu, B., Jin, L., Li, Y., Shi, Z., Yan, H., Hu, H., 2016. Interaction between Hydrogen-Donor and Nondonor Solvents in Direct Liquefaction of Bulianta Coal. Energy Fuels 30, 10260–10267.

Ntakirutimana, S., Xu, T., Liu, H., Cui, J.-Q., Zong, Q.-J., Liu, Z.-H., Li, B.-Z., Yuan, Y.-J., 2022. Amine-based pretreatments for lignocellulose fractionation and lignin valorization: a review. Green. Chem. 24, 5460–5478.

Qian, Y., Zhang, F., Pang, H., 2021. A Review of MOFs and Their Composites-Based Photocatalysts: Synthesis and Applications. Adv. Funct. Mater. 31, 2104231.

Rajesh Banu, J., Kavitha, S., Yukesh Kannah, R., Poornima Devi, T., Gunasekaran, M., Kim, S.-H., Kumar, G., 2019. A review on biopolymer production via lignin valorization. Bioresour. Technol. 290, 121790.

Sabzehmeidani, M.M., Gafari, S., jamali, S., Kazemzad, M., 2024. Concepts, fabrication and applications of MOF thin films in optoelectronics: A review. Appl. Mater. Today 38, 102153.

Sun, Z., Fridrich, B., de Santi, A., Elangovan, S., Barta, K., 2018. Bright Side of Lignin Depolymerization: Toward New Platform Chemicals. Chem. Rev. 118, 614–678.

Vernekar, D., Dayyan, M., Ratha, S., Rode, C.V., Haider, M.A., Khan, T.S., Jagadeesan, D., 2021. Direct Oxidation of Cyclohexane to Adipic Acid by a WFeCoO(OH) Catalyst: Role of Brønsted Acidity and Oxygen Vacancies. ACS Catal. 11, 10754–10766.

Wang, K., Li, Y., Xie, L.-H., Li, X., Li, J.-R., 2022. Construction and application of base-stable MOFs: a critical review. Chem. Soc. Rev. 51, 6417–6441.

Wu, X., Li, H., Ge, F., Xu, W., Lu, H., Zhou, M., 2024. N-doped MOF-lignin hybrid catalyst for highly selective hydrodeoxygenation of lignin-derived phenols. Chem. Eng. J. 495, 153009.

Xia, H., Li, J., Chen, C., Wu, D., Ren, J., Jiang, J., Zhou, M., 2021. Selective aqueous-phase hydrogenation of furfural to cyclopentanol over Ni-based catalysts prepared from Ni-MOF composite. Inorg. Chem. Commun. 133, 108894.

Xie, J.-X., Zhao, Y.-P., Li, Q., Qiu, L.-L., Liu, F.-J., Liang, J., Li, J., Cao, J.-P., 2024. Highly efficient conversion of lignin bio-oil and derived phenols to cyclohexanols over low-loading Ni/C catalyst. Fuel 371, 132030.

Xue, Z., Sun, H., Wang, G., Sui, W., Jia, H., Si, C., 2024. Fabrication modulation of lignin-derived carbon nanosphere supported Pd nanoparticle via lignin fractionation for improved catalytic performance in vanillin hydrodeoxygenation. Int. J. Biol. Macromol. 258, 128963.

Yang, X., Niu, L., Xia, Z., Yan, X., Bai, G., 2020. Preparation of Ni/$mSiO_2$ with the existence of hydrogelator: Insight into hydrogelator self-assembly on metal dispersion and catalytic performance in quinoline hydrogenation. Mol. Catal. 493.

Yue, X., Zhang, S., Shang, N., Gao, S., Wang, Z., Wang, C., 2020. Porous organic polymer supported PdAg bimetallic catalyst for the hydrodeoxygenation of lignin-derived species. Renew. Energy 149, 600–608.

Zeng, Y., Lin, L., Hu, D., Jiang, Z., Saeed, S., Guo, R., Ashour, I., Yan, K., 2023. Highly dispersed Ru nanoparticles anchored on NiAl layered double oxides catalyst for selective hydrodeoxygenation of vanillin. Catal. Today 423, 114252.

Zhai, W., Chen, Y., Liu, Y., Sakthivel, T., Ma, Y., Qin, Y., Qu, Y., Dai, Z., 2023. Enlarging the Ni–O Bond Polarizability in a Phosphorene-Hosted Metal–Organic Framework for Boosted Water Oxidation Electrocatalysis. ACS Nano 17, 17254–17264.

Zhang, J., Wang, L., Hu, X., Shao, Q., Xu, X., Long, C., 2021. Balancing surface acidity, oxygen vacancies and Cu^+ of CuOx/CeO_2 catalysts by Nb doping for enhancing CO oxidation and moisture resistance and lowering byproducts in plasma catalysis. J. Clean. Prod. 318, 128564.

Zhang, Y., Naebe, M., 2021. Lignin: A Review on Structure, Properties, and Applications as a Light-Colored UV Absorber. ACS Sustain. Chem. Eng. 9, 1427–1442.

Zhang, Z., Cao, J., Wang, S., Sun, Z., Li, J., 2023. Enhanced Sensitivity of $ZnFe_2O_4$ Based on Ordered Magnetic Moment Induced by Magnetic Field: A New Insight into Mechanism. Adv. Funct. Mater. 33, 2305253.

Zhou, M., Tang, C., Li, J., Xia, H., Liu, P., Xu, J., Chen, C., Jiang, J., 2022a. Spherical NiCo-MOFs catalytic hydrogenolysis of lignin dimers and enzymatic lignin to value-added liquid fuels under nitrogen atmosphere. Fuel 315, 123156.

Zhou, R., Mohamedali, M., Ren, Y., Lu, Q., Mahinpey, N., 2022b. Facile synthesis of multi-layered nanostructured Ni/CeO2 catalyst plus in-situ pre-treatment for efficient dry reforming of methane. Appl. Catal. B: Environ. 316, 121696.